

# Plug-and-Hide: Provable and Adjustable Diffusion Generative Steganography

Jiahao Zhu, Zixuan Chen, Lingxiao Yang, *Member, IEEE*, Xiaohua Xie, *Member, IEEE*, Yi Zhou

**Abstract**—Generative Steganography (GS) is a novel technique that utilizes generative models to conceal messages without relying on cover images. Contemporary GS algorithms leverage the powerful generative capabilities of Diffusion Models (DMs) to create high-fidelity stego images. However, these algorithms, while yielding relatively satisfactory generation outcomes and message extraction accuracy, significantly alter modifications to the initial Gaussian noise of DMs, thereby compromising steganographic security. In this paper, we rethink the trade-off among image quality, steganographic security, and message extraction accuracy within Diffusion Generative Steganography (DGS) settings. Our findings reveal that the normality of initial noise of DMs is crucial to these factors and can offer theoretically grounded guidance for DGS design. Based on this insight, we propose a Provable and Adjustable Message Mapping (PA-B2G) approach. It can, on one hand, theoretically guarantee reversible encoding of bit messages from arbitrary distributions into standard Gaussian noise for DMs. On the other hand, its adjustability provides a more natural and fine-grained way to trade off image quality, steganographic security, and message extraction accuracy. By integrating PA-B2G with a probability flow ordinary differential equation, we establish an invertible mapping between secret messages and stego images. PA-B2G can be seamlessly incorporated with most mainstream DMs, such as the Stable Diffusion, without necessitating additional training or fine-tuning. Comprehensive experiments corroborate our theoretical insights regarding the trade-off in DGS settings and demonstrate the effectiveness of our DGS algorithm in producing high-quality stego images while preserving desired levels of steganographic security and extraction accuracy.

**Index Terms**—Generative steganography, diffusion models, ordinary differential equation.

## I. INTRODUCTION

STEGANOGRAPHY, as both an art and a science, aims to conceal secret data within seemingly innocuous objects, such as images, to implement covert communication. In traditional image steganography, the process typically starts by selecting benign images (*a.k.a.* cover images) as message containers and embedding secret messages into their least significant bits using either non-adaptive embedding [1] or

Manuscript received XXXX XX, XXXX; revised XXXX XX, XXXX. This work was supported in part by the National Natural Science Foundation of China (12326618, U22A2095) and the Project of Guangdong Provincial Key Laboratory of Information Security Technology (2023B1212060026).

Corresponding author: Xiaohua Xie and Yi Zhou.

Jiahao Zhu, Zixuan Chen, Lingxiao Yang, and Xiaohua Xie are with the School of Computer Science and Engineering, Sun Yat-sen University, and with the Guangdong Province Key Laboratory of Information Security Technology, and also with the Key Laboratory of Machine Intelligence and Advanced Computing, Ministry of Education, 510006, Guangzhou, China (e-mail: {zhujh59, chenzx3}@mail2.sysu.edu.cn; {yanglx9, xiexiangoh6}@mail.sysu.edu.cn);. Yi Zhou is with the Zhongshan School of Medicine, Sun Yat-sen University (e-mail: zhouyi@mail.sysu.edu.cn).

adaptive embedding methods [2]. However, these algorithms generally offer limited message embedding capacity. Furthermore, even with low payloads, the act of concealing messages inevitably introduces statistical anomalies between the cover images and their stego counterparts, heightening the risk of detection by machine learning-based steganalysis [3]–[6].

To address these challenges, a novel technique called Generative Steganography (GS) has emerged. Unlike conventional image steganography, GS leverages generative models to create stego images directly from secret messages, eliminating the need for predefined containers. Early GS algorithms [7]–[16] primarily utilize Generative Adversarial Networks (GANs) [17] and Flow models [18] as foundational frameworks for producing stego images. GAN-based methods [7]–[14] typically require training three networks simultaneously: a generator, a discriminator, and a message extractor. This necessitates a delicate balance between stego image generation and message extraction during training, which increases the training complexity and often leads to suboptimal generation outcomes and message extraction accuracy. Conversely, Flow-based methods [15], [16] exploit the reversibility of Flow networks to establish a bijective mapping between secret messages and stego images. However, this stringent reversibility also constrains their image generation capabilities.

Recently, Diffusion Models (DMs) [19]–[21], constructed from a hierarchy of denoising autoencoders, have demonstrated remarkable results in both unconditional and conditional image synthesis. These models iteratively denoise Gaussian white noise to generate high-quality images. Building on this approach, recent studies [22], [23] have utilized pre-trained DMs for stego image generation. These methods heuristically devise various message mapping strategies to transform secret messages into quasi-Gaussian noise, which is then used as the input for DMs. By constructing an Ordinary Differential Equation (ODE), the noise and its corresponding generated stego image can be converted into each other through an approximate solver of the ODE, such as the Euler method. While these methods achieve superior generation quality and message extraction accuracy compared to GAN- and Flow-based methods, their arbitrary embedding modifications to the initial noise of DMs compromise its normality, resulting in suboptimal generation outcomes and reduced steganographic security, despite their claims of security. This underscores two fundamental issues: the specific correlation among image quality, steganographic security, and message extraction accuracy, and the challenge of trading off these aspects. Although [22] has experimentally identified a trade-off between image quality and extraction accuracy in DGS, it

does not consider the security.

To address these issues, this paper presents theoretical evidence revealing the underlying correlations among image quality, extraction accuracy, and steganographic security. We assert that the key to balancing these three factors lies in the normality level of the generated initial noise for DMs. Specifically, image quality and steganographic security are positively correlated with the normality level, while message extraction accuracy is negatively correlated. This implies that any action compromising the normality of the initial noise in DMs will result in degraded image quality and reduced steganographic security. Thus, [22], [23] are not as secure as they claim to be. Based on our findings, we propose a provable and adjustable message mapping method, dubbed PA-B2G, which can reversibly transform any bit message into standard Gaussian noise. PA-B2G comprises two stages: **i**) mapping arbitrary secret bits to uniformly sampled noise based on a symmetric interval partitioning strategy, and **ii**) generating standard Gaussian noise via the Inverse Transform Sampling. Moreover, we introduce no-sampling intervals and propose a variance-preserving algorithm, providing a more natural and fine-grained way to trade off image quality, steganographic security, and extraction accuracy. By combining PA-B2G with a probability flow ODE, we establish an invertible mapping between secret messages and stego images. This approach allows PA-B2G to seamlessly integrate with most mainstream DMs without the need for additional training or fine-tuning. The contributions of our work are fourfold:

- To the best of our knowledge, this is the first work to provide theoretical evidence of the correlation among image quality, steganographic security, and message extraction accuracy in DGS settings.
- Based on our theoretical analysis, we propose PA-B2G, which can be proven to reversibly transform any secret message into standard Gaussian noise. Additionally, its adjustability offers a natural and fine-grained way to trade off image quality, steganographic security, and message extraction accuracy.
- PA-B2G decouples message embedding, stego image generation, and message extraction. This allows it to be directly combined with most off-the-shelf DMs without any training or fine-tuning, achieving a plug-and-hide effect.
- Extensive experiments validate the correctness of our exploration regarding the trade-off in DGS settings and demonstrate the efficacy of our DGS algorithm in generating high-quality stego images while maintaining desirable steganographic security and extraction accuracy.

The remainder of the paper is organized as follows. Sec. II provides a brief overview of existing DGS algorithms. Sec. III discusses the preliminary knowledge on the probability flow ODE used in DMs and the general DGS framework. Sec. IV investigates the correlation among image quality, steganographic security, and message extraction accuracy, and introduces our PA-B2G approach. Sec. V presents the experimental results. Finally, Sec. VI summarizes the conclusions and limitations of our work.

## II. RELATED WORK

GS is a novel technique for concealing messages within generated images using generative models. Unlike traditional steganography, which embeds secret messages into existing images, GS generates new stego images from scratch, inherently integrating the secret messages into the creation process. Existing GS methods can be broadly classified into three categories:

**GAN-based algorithms.** Liu *et al.* [7] pioneered GAN-based steganography by replacing class labels with secret data to synthesize stego images. Hu *et al.* [8] employed GANs to translate secret data into noise vectors for generating carrier images. Wang *et al.* [9] introduced a self-learning GAN-based approach for direct stego image generation from secret messages. Yu *et al.* [10] proposed an attention-GAN method with optimized network architecture and loss functions. Despite advancements, these methods often suffer from challenges such as low image quality and poor message extraction accuracy. In response, Liu *et al.* [11] introduced an image disentanglement autoencoder for GS, enhancing both image generation quality and message extraction accuracy. Wei *et al.* [12] incorporated a mutual information mechanism to improve extraction accuracy and designed a hierarchical gradient decay technique to enhance anti-steganalysis capabilities. Addressing robustness issues in recovery and synthesis quality, Ma *et al.* [13] developed a weight modulation-based generator and a difference predictor for enhanced extraction robustness. Most recently, Zhou *et al.* [14] identified security vulnerabilities in the feature domain of existing GAN-based GS algorithms. They proposed a framework that auto-generates semantic object contours to enhance security in GS applications.

**Flow-based algorithms.** To achieve a higher embedding capacity and enhance message extraction accuracy, Wei *et al.* [15] introduced a novel Flow-based GS algorithm. This method directly embeds secret messages within the binarized initial noise of a trained Glow model. In a related approach, Zhou *et al.* [16] proposed the Secret-to-Image Reversible Transformation (S2IRT). This technique utilizes permutation steganography to encode secret bits by rearranging the order of entries in Glow latent vectors.

**Diffusion-based algorithms.** With the advent of DMs (Deep Models), Wei *et al.* [23] introduced Generative Steganography Diffusion (GSD), a technique leveraging Denoising Diffusion Implicit Models (DDIMs) [24]. This method hides bits within the frequency domain of the initial Gaussian noise of DDIMs. In a related development, Kim *et al.* [22] devised four message projection methods: Message to Noise (MN), Message to Binary (MB), Message to Centered Binary (MC), and Multi-bits. These methods transform secret messages into noise suitable for input into pre-trained DMs. Additionally, Peng *et al.* [25] proposed StegaDDPM, a novel GS algorithm based on the denoising diffusion probabilistic model (DDPM) [26]. StegaDDPM utilizes the probability distribution between intermediate states and generated images of DDPM to embed secret information.

### III. PRELIMINARY

To avoid confusion, variables in the paper are denoted as follows: bold lowercase letters signify vectors, bold uppercase letters signify tensors, and regular font indicates scalars.

**Probability flow ODE.** Chen *et al.* [27] propose a neural network ODE as a replacement for earlier residual networks, recurrent neural network decoders, and normalizing flows. The ODE is defined as follows:

$$\dot{\mathbf{x}}(t) = f(\mathbf{x}(t), t), \quad (1)$$

where the dot denotes a time derivative. Eq. (1) is now commonly seen in recent diffusion model [24], [28], [29], and is widely used for image generation. Recently, Karras *et al.* [30] enrich Eq. (1) into

$$\dot{\mathbf{x}}(t) = \frac{\dot{s}(t)}{s(t)} - s(t)^2 \dot{\sigma}(t) \sigma(t) \nabla_{\mathbf{x}} p(\frac{\mathbf{x}}{s(t)}; \sigma(t)), \quad (2)$$

where  $s(t)$  and  $\sigma(t)$  represent scale value and noise value at time  $t$ , respectively, and  $\nabla_{\mathbf{x}}(\cdot)$  denotes a time-dependent gradient field (*a.k.a.* score function) which points to higher density of data  $\mathbf{x}$ . Eq. (2) is also known as probability flow ODE because, assuming that the integral interval of Eq. (2) is set to  $[0, T]$ , one can generate an image  $\mathbf{x}_0$  by integrating Eq. (2) along the time direction of  $T$  to 0, and likewise, one can regain  $\mathbf{x}_T$  by integrating Eq. (2) in the opposite direction. The initial noise  $\mathbf{x}_T \sim \mathcal{N}(\mathbf{0}, \sigma(T)^2 \mathbf{I})$ , as proven in [30]. Since data sampled from  $\mathbf{x}_T \sim \mathcal{N}(\mathbf{0}, \sigma(T)^2 \mathbf{I})$  can be derived by that from  $\mathcal{N}(\mathbf{0}, \mathbf{I})$  through reparameterization, for simplicity, we consider  $\mathbf{x}_T \sim \mathcal{N}(\mathbf{0}, \mathbf{I})$  in the following sections. In practice, one can independently sample multiple times from  $\mathcal{N}(0, 1)$  to form  $\mathbf{x}_T$ .

**General DGS framework.** A classical steganography system involves Alice and Bob as primary actors, each of whom possesses the authority to transmit seemingly innocuous images across a public channel. Additionally, the system also has a vigilant observer named Eve, who maintains all-seeing, read-only surveillance over the channel. Alice and Bob's main goal is to evade Eve's scrutiny while covertly exchanging secret messages. In DGS settings, Alice and Bob utilize the invertibility of Eq. (2) to exchange secret messages. Specifically, one side first follows the Kerckhoffs's principle [31] to commence the process by encrypting message bits with shared keys. Next, he or she encodes the ciphertext into a Gaussian noise  $\mathbf{g}$  by noise modification or direct message mapping. The procedure of generating stego images involves integrating Eq. (2) from  $\mathbf{g}$  to  $\mathbf{x}_0$ . Conversely, the message retrieval is realized by inverting the generation procedure. The general workflow of DGS system is illustrated in Fig. 1.

### IV. OUR METHOD

In Sec. IV-A1, we reconsider the trade-off among security, image quality, and extraction accuracy in DGS settings, and further theoretically explore the correlations between the latent normality and these three factors. Motivated by this, we propose our PA-B2G mapping method, which is elaborated on in Sec. IV-B and Sec. IV-C. The entire message hiding and extraction procedure based on ODE sampling are described in Sec. IV-D.

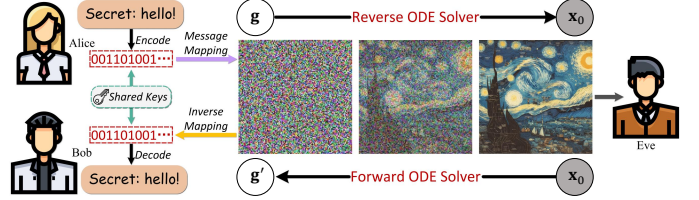


Fig. 1: The general DGS framework.

#### A. Hub among Security, Image Quality, and Extraction Accuracy

In this section, we argue that the normality level of the constructed latent noise  $\mathbf{g}$  serves as the hub among security, image quality, and extraction accuracy.

##### 1) Correlation with security and image quality:

**Definition 1.** According to [32], given the cover image distribution  $p_c(\mathbf{x})$  and stego image distribution  $p_s(\mathbf{x})$ , the definition of steganographic security posits that a stegosystem is considered perfectly secure when  $D_{KL}(p_c(\mathbf{x})||p_s(\mathbf{x})) = 0$ , and  $\epsilon$ -secure if  $D_{KL}(p_c(\mathbf{x})||p_s(\mathbf{x})) \leq \epsilon$ .

**Theorem 1.** In DGS settings, let  $\mathcal{O}$  denotes the forward mapping of Eq. (2), cover image  $\mathbf{x}_c \sim p_c(\mathbf{x})$ , and stego image  $\mathbf{x}_s \sim p_s(\mathbf{x})$ . Initial noise  $\mathbf{g}_c = \mathcal{O}(\mathbf{x}_c)$  and  $\mathbf{g}_s = \mathcal{O}(\mathbf{x}_s)$ . In theory,  $D_{KL}(p_c(\mathbf{x})||p_s(\mathbf{x})) = D_{KL}(p_c(\mathbf{g})||p_s(\mathbf{g}))$  holds.

*Proof.* Let  $\mathcal{X}$  denote the image space, we have

$$\begin{aligned} D_{KL}(p_c(\mathbf{x})||p_s(\mathbf{x})) &= \sum_{\mathbf{x} \in \mathcal{X}} p_c(\mathbf{x}) \log \frac{p_c(\mathbf{x})}{p_s(\mathbf{x})} \\ &= \sum_{\mathbf{g} \in \mathcal{O}(\mathcal{X})} \sum_{\mathbf{x} \in \mathcal{O}^{-1}(\mathbf{g})} p_c(\mathbf{x}) \log \frac{p_c(\mathbf{x})}{p_s(\mathbf{x})}. \end{aligned} \quad (3)$$

Let  $\mathcal{O}^{-1}(\mathbf{g}) = \{\mathbf{x}_1, \dots, \mathbf{x}_k\}$ , we have

$$\sum_{\mathbf{x} \in \mathcal{O}^{-1}(\mathbf{g})} p_c(\mathbf{x}) \log \frac{p_c(\mathbf{x})}{p_s(\mathbf{x})} = \sum_{i=1}^k p_c(\mathbf{x}_i) \log \frac{p_c(\mathbf{x}_i)}{p_s(\mathbf{x}_i)}. \quad (4)$$

According to the log sum inequality, we can easily get

$$\sum_{i=1}^k p_c(\mathbf{x}_i) \log \frac{p_c(\mathbf{x}_i)}{p_s(\mathbf{x}_i)} \geq \sum_{i=1}^k p_c(\mathbf{x}_i) \log \frac{\sum_{j=1}^k p_c(\mathbf{x}_j)}{\sum_{j=1}^k p_s(\mathbf{x}_j)}. \quad (5)$$

As  $\mathbf{g} \in \mathcal{O}(\mathcal{X})$ ,  $p_c(\mathbf{g}) = \sum_{\mathbf{x} \in \mathcal{O}^{-1}(\mathbf{g})} p_c(\mathbf{x})$ , and similarly,  $p_s(\mathbf{g}) = \sum_{\mathbf{x} \in \mathcal{O}^{-1}(\mathbf{g})} p_s(\mathbf{x})$ . In summary, we have

$$\begin{aligned} D_{KL}(p_c(\mathbf{x})||p_s(\mathbf{x})) &\geq \\ &\sum_{\mathbf{g} \in \mathcal{O}(\mathcal{X})} \sum_{i=1}^k p_c(\mathbf{x}_i) \log \frac{\sum_{j=1}^k p_c(\mathbf{x}_j)}{\sum_{j=1}^k p_s(\mathbf{x}_j)} \\ &= \sum_{\mathbf{g} \in \mathcal{O}(\mathcal{X})} p_c(\mathbf{g}) \log \frac{p_c(\mathbf{g})}{p_s(\mathbf{g})} = D_{KL}(p_c(\mathbf{g})||p_s(\mathbf{g})). \end{aligned} \quad (6)$$

As mapping  $\mathcal{O}$  is invertible, we can use the same method described above to obtain

$$D_{KL}(p_c(\mathbf{g})||p_s(\mathbf{g})) \geq D_{KL}(p_c(\mathbf{x})||p_s(\mathbf{x})). \quad (7)$$

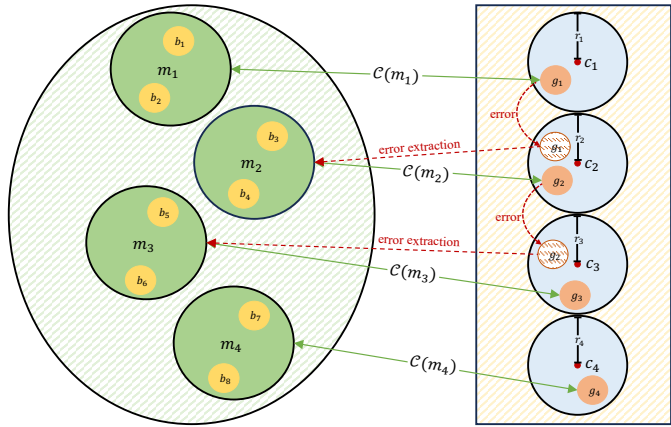


Fig. 2: An illustrative example of  $\mathcal{C}(m) = g$  with  $l = 2$ . Assuming that data in blue regions follows  $\mathcal{N}(0, 1)$ ,  $m$  should be independently mapped into the blue regions so that *i.i.d.*  $g \sim \mathcal{N}(0, 1)$ .

Combining Eq. (6) and Eq. (7),  $D_{KL}(p_c(\mathbf{x})||p_s(\mathbf{x})) = D_{KL}(p_c(\mathbf{g})||p_s(\mathbf{g}))$  holds.  $\square$

Thm. 1 suggests that as the distribution of the crafted noise deviates from  $p_c(\mathbf{g}) := \mathcal{N}(\mathbf{0}, \mathbf{I})$ ,  $D_{KL}(p_c(\mathbf{x})||p_s(\mathbf{x}))$  gradually rises, signaling a decrease in steganographic security and image quality, underscoring the significance of preserving the normality of  $\mathbf{g}$  in DGS system.

2) *Correlation with extraction accuracy:* However, simply preserving the normality of  $\mathbf{g}$  also compromises the extraction accuracy (and vice versa), which can be explained from the perspective of coding theory. Specifically, given an source code  $\mathcal{C}$  that maps a bit sequence  $\mathbf{b} = b_1 b_2 \cdots b_n$  to random noise  $\mathbf{g} = g_1 g_2 \cdots g_k$  with  $g_i \sim \mathcal{N}(0, 1)$ .  $\mathbf{b}$  can be further divided into several subsequences of length  $l$  ( $l \geq 1$ ), forming an integer sequence  $\mathbf{m} = m_1 m_2 \cdots m_k$  with  $m_i \in \{0, 1, \dots, 2^l - 1\}$ . Since message encryption is performed beforehand,  $m_i$  are *i.i.d.*. The mapping procedure can be defined by  $\mathcal{C}(m) = g = c + \epsilon^l$ , where  $c$  and  $\epsilon$  are deterministic center points and random offsets, respectively, and  $D(g, c) \leq r$  with  $r \geq 0$ . If we want to extract secret bits (regardless of whether errors occur),  $\mathcal{C}^{-1}$  is at least a surjective non-injective function. Fig. 2 shows an illustrative example:  $g \sim \mathcal{N}(0, 1)$  in disjoint blue regions, and  $g_i$  satisfying  $D(g_i, c_i) \leq r_i$  can be decoded to unique bit sequence. However, when errors occur, e.g.,  $g_1$  falls into the circle centered at  $c_2$ , resulting in extraction error. One way to alleviate this problem is by increasing the distance between the central points  $c$ , while the other is by reducing the radii  $r$  of blue circles, both of which undoubtedly compromises the normality of  $\mathbf{g}$ .

### B. Provable PA-B2G

To reversibly convert any encrypted bit messages to Gaussian noise, we heuristically design a two-stage message mapping approach named PA-B2G. In the first stage, any encrypted bit messages to uniformly distributed noise, which can be

<sup>1</sup>We omit the subscripts of  $b$  and  $g$  here because  $\mathcal{C}$  has no difference across varying  $m_i$ .

expressed by  $\mathcal{C}_u(m) = u$  with  $u \sim \mathcal{U}(0, 1)$ . Note that the notations used here are consistent with those defined in Sec. IV-A2. Inspired by arithmetic coding, we implement such a mapping via a symmetrical interval partitioning strategy. Specifically, we propose two intuitive partition modes:

- I. The interval  $[0, 1]$  is evenly partitioned into  $2^l$ , and  $u$  is sampled from  $\mathcal{U}(\frac{m}{2^l}, \frac{m+1}{2^l})$ .
- II. The interval  $[0, 1]$  is evenly partitioned into  $2^{l+1}$ , and  $u$  is sampled from  $\mathcal{U}(\frac{m}{2^{l+1}}, \frac{m+1}{2^{l+1}})$  or  $\mathcal{U}(1 - \frac{m+1}{2^{l+1}}, 1 - \frac{m}{2^{l+1}})$ .

In the second stage, the obtained  $u$  is transformed into Gaussian noise  $g$  by the Inverse Transform Sampling, which can be expressed by  $g = \mathcal{C}_g(u)$  with  $\mathcal{C}_g$  denoting the percent point function (PPF) w.r.t.  $\mathcal{N}(0, 1)$ .

By iterating the aforementioned two steps, we can obtain the final noise sequence  $\mathbf{g}$ . The implementation details of PA-B2G and its inverse procedure are provided in Alg. 1 and Alg. 2, respectively. Note that intervals partitioned by the two modes are all symmetric about  $u = \frac{1}{2}$ , which is the reason we refer to our method as the symmetrical interval partition, and its rationale is discussed in the next section. Here we first demonstrate the normality of the generated noise  $\mathbf{g}$ .

**Theorem 2.** *Given a message sequence  $\mathbf{m} = m_1 m_2 \cdots m_k$ , the noise sequence  $\mathbf{g} = g_1 g_2 \cdots g_k$  generated by PA-B2G follows  $\mathcal{N}(\mathbf{0}, \mathbf{I})$ .*

*Proof.*  $p(g) = \sum_m p(g|m)p(m)$ . Since  $\mathbf{m}$  is encrypted beforehand,  $p(m) = 2^{-l}$ , and

$$\begin{aligned} p(g|m) &= \int p(g, u|m)du = \int p(g|u, m)p(u|m)du \\ &= p(g|\mathcal{C}_u(m))p(\mathcal{C}_u(m)). \end{aligned} \quad (8)$$

For the mode I,

$$\begin{aligned} p(g|m) &= p(g|\mathcal{C}_u(m))p(\mathcal{C}_u(m)) = \frac{2^l p(g|\mathcal{C}_u(m))}{(m+1-m)} \\ &= \begin{cases} \frac{2^l}{\sqrt{2\pi}} e^{-\frac{g^2}{2}} & \text{if } g \in [\mathcal{C}_g(\frac{m}{2^l}), \mathcal{C}_g(\frac{m+1}{2^l})] \\ 0 & \text{otherwise.} \end{cases} \end{aligned} \quad (9)$$

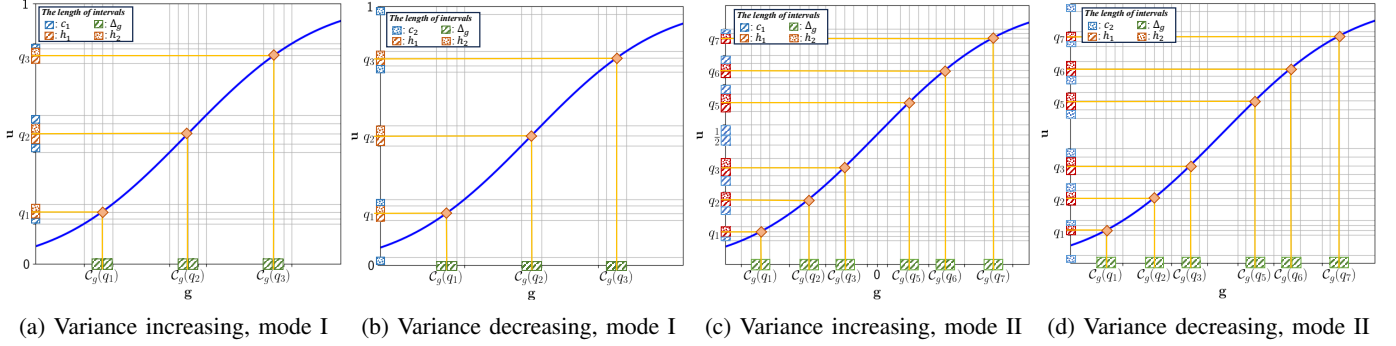
According to Eq. (8),

$$\begin{aligned} p(g) &= p(g|m)p(m) = \frac{1}{2^l} \sum_m p(g|m)p(m) \\ &= \sum_m p(g|\mathcal{C}_u(m)) = \frac{1}{\sqrt{2\pi}} e^{-\frac{g^2}{2}} := \mathcal{N}(0, 1), g \in \mathbb{R}. \end{aligned} \quad (10)$$

For the mode II,

$$\begin{aligned} p(g|m) &= p(g|\mathcal{C}_u(m))p(\mathcal{C}_u(m)) = \frac{2^{l+1} p(g|\mathcal{C}_u(m))}{2(m+1-m)} \\ &= \begin{cases} \frac{2^l}{\sqrt{2\pi}} e^{-\frac{g^2}{2}} & \text{if } g \in [\mathcal{C}_g(\frac{m}{2^{l+1}}), \mathcal{C}_g(\frac{m+1}{2^{l+1}})], \\ \frac{2^l}{\sqrt{2\pi}} e^{-\frac{g^2}{2}} & \text{if } g \in [\mathcal{C}_g(1 - \frac{m+1}{2^{l+1}}), \mathcal{C}_g(1 - \frac{m}{2^{l+1}})], \\ 0 & \text{otherwise.} \end{cases} \end{aligned} \quad (11)$$

similarly, we can obtain  $p(g) = \frac{1}{\sqrt{2\pi}} e^{-\frac{g^2}{2}} := \mathcal{N}(0, 1)$ , where  $g \in \mathbb{R}$ . Since  $g_i$  are *i.i.d.*,  $p(\mathbf{g}) = \prod_{i=1}^k p(g_i) = \frac{1}{(2\pi)^{k/2}} e^{-\frac{1}{2} \mathbf{g}^T \mathbf{g}} := \mathcal{N}(\mathbf{0}, \mathbf{I})$ .  $\square$



(a) Variance increasing, mode I (b) Variance decreasing, mode I (c) Variance increasing, mode II (d) Variance decreasing, mode II

Fig. 3: Examples of  $l = 2$  for modes I and II. Along the vertical axis in each figure, the red regions represent the neighborhoods of quantiles, and the blue regions represent the variance-correction intervals. Sampling within these regions is prohibited. The green regions are the intervals that we actually adjust. Our variance-preserving strategy in each iteration involves two key steps: (a) increasing  $S_u^2$  by increasing  $c_1$ , and (b) decreasing  $S_u^2$  by increasing  $c_2$ .

### Algorithm 1 PA-B2G

**Input:** Secret message  $\mathbf{m}$ .

**Output:** Noise  $\mathbf{g}$ .

```

1: for  $i = 1$  to  $k$  do
2:   Sample  $r_i \sim \mathcal{U}(0, 1)$ ;
3:    $u_i = \frac{r_i}{2^l} + \frac{m_i}{2^l}$ ;  $\triangleright$  mode I
4:    $u_i = \frac{r_i}{2^{l+1}} + \frac{m_i}{2^{l+1}}$  or  $u_i = \frac{r_i}{2^{l+1}} + 1 - \frac{m_i+1}{2^{l+1}}$ ;  $\triangleright$  mode II
5:    $g_i = \mathcal{C}_g(u_i)$ ;
6:    $\mathbf{g} = g_1 g_2 \cdots g_k$ ;
7: Return  $\mathbf{g}$ .
```

### Algorithm 2 Inverse Procedure of PA-B2G

**Input:** Noise  $\mathbf{g}$ .

**Output:** Secret message  $\mathbf{m}$ .

```

1: for  $i = 1$  to  $k$  do
2:    $u_i = \mathcal{C}_g^{-1}(g_i)$ ;
3:    $m_i = \lfloor u_i 2^l \rfloor$ ;  $\triangleright$  mode I
4:    $m_i = \lfloor (1 - u_i) 2^{l+1} \rfloor$  if  $u_i > 0.5$  else  $\lfloor u_i 2^{l+1} \rfloor$ ;  $\triangleright$  mode II
5:    $\mathbf{m} = m_1 m_2 \cdots m_k$ ;
6: Return  $\mathbf{m}$ .
```

Furthermore, the following proposition holds:

**Proposition 1.** *In theory, PA-GPA can makes our GS algorithm achieve perfect security.*

*Proof.* According to Definition 1, Thm. 1, and Thm. 2, we can derive that  $D_{KL}(p_c(\mathbf{g})||p_s(\mathcal{C}_g \circ \mathcal{C}_u(\mathbf{m}))) = D_{KL}(P_c(\mathbf{x})||p_s(\mathcal{O}^{-1} \circ \mathcal{C}_g \circ \mathcal{C}_u(\mathbf{m}))) = 0$   $\square$

### C. Adjustable PA-B2G

Sec. IV-B demonstrates that PA-G2B can generate standard Gaussian noise and theoretically is perfectly secure. However, in practical scenarios, discrete numerical solutions to ODEs and image quantization both introduce errors in message extraction [22], [23]. We observe that changes in  $u$  within the  $h$ -neighborhoods of the quantiles (defined in Thm. 3) are more likely to cause extraction errors. Considering the conclusion

drawn in Sec. IV-A2, we have to slightly compromise the Gaussian nature of  $\mathbf{g}$  to improve extraction accuracy.

One straightforward but effective solution is to avoid sampling within these neighborhoods, which aligns with the approach proposed in Sec. IV-A2. However, this may alter the statistical characteristics of the sample  $\mathbf{g}$ , potentially compromising the stego image generation. According to [22], to achieve decent image generation results, at least the following three conditions must be satisfied: **i**) the sample mean of  $\mathbf{g}$  must be close to 0; **ii**) the sample variance must be close to 1; **iii**) all  $g_i$  should be *i.i.d.*. Inspired by this, we propose a variance-preserving algorithm. Before proceeding further, we need to consider the following conclusions.

**Theorem 3.** *Let  $\mathbf{q} = \{q_i|_{\frac{i}{2^l}}, i = 1, \dots, 2^l - 1\}$  and  $\tilde{\mathbf{q}} = \{\tilde{q}_i|_{\frac{i}{2^{l+1}}}, i = 1, \dots, 2^{l+1} - 1, i \neq 2^l\}$  denote the quantile sets w.r.t. partitioning mode I and II, respectively. Assuming that sampling in the  $h$ -neighborhoods of these quantiles, which are expressed as  $(q_i - h, q_i + h)$  for mode I and  $(\tilde{q}_i - h, \tilde{q}_i + h)$  for mode II, is prohibited, we have  $\bar{g} = \frac{1}{k} \sum_{i=1}^k g_i = 0$  and  $S_g^2 = \frac{1}{k-1} \sum_{i=1}^k (g_i - \bar{g})^2 \neq 1$ .*

*Proof.* According to Thm. 2,

$$\begin{aligned}
p(g) &= \sum_m p(g|\mathcal{C}_u(m))p(\mathcal{C}_u(m))p(m) \\
&= \frac{1}{2^l} \sum_m p(g|\mathcal{C}_u(m))p(\mathcal{C}_u(m)).
\end{aligned} \tag{12}$$

For the mode I,

$$p(g) = \begin{cases} 0, & g \in \bigcup_{i=1}^{2^l-1} (\mathcal{C}_g(q_i - h), \mathcal{C}_g(q_i + h)). \\ \frac{2^l-h}{2^l\sqrt{2\pi}} e^{-\frac{g^2}{2}}, & g \in (-\infty, \mathcal{C}_g(q_1-h)) \cup (\mathcal{C}_g(q_{2^l-1}+h), +\infty), \\ \frac{2^l-2h}{2^l\sqrt{2\pi}} e^{-\frac{g^2}{2}}, & \text{otherwise.} \end{cases} \tag{13}$$

As for the mode II,

$$p(g) = \begin{cases} 0, & g \in \bigcup_{i=1, i \neq 2^l}^{2^{l+1}-1} (\mathcal{C}_g(\tilde{q}_i - h), \mathcal{C}_g(\tilde{q}_i + h)). \\ \frac{2^l - 2h}{2^l \sqrt{2\pi}} e^{-\frac{g^2}{2}}, & g \in (-\infty, \mathcal{C}_g(\tilde{q}_1 - h)) \cup (\mathcal{C}_g(\tilde{q}_{2^{l+1}-1} + h), +\infty) \\ \frac{2^l \sqrt{2\pi}}{2^l} e^{-\frac{g^2}{2}}, & \cup (\mathcal{C}_g(\tilde{q}_{2^l-1} + h), \mathcal{C}_g(\tilde{q}_{2^l+1} - h)), \\ \frac{2^l - 4h}{2^l \sqrt{2\pi}} e^{-\frac{g^2}{2}}, & \text{otherwise.} \end{cases} \quad (14)$$

According to Eq. (13) and Eq. (14), the following conclusions hold true for both modes I and II: **i**)  $gp(g)$  is an odd function; **ii**) the integral interval is symmetric about the axis  $g = 0$ ; and **iii**) the functions  $gp(g)$  is bounded and contains a finite number of jump discontinuities within the integral interval. By considering these conditions collectively, we can derive that  $E[g] = \int_{-\infty}^{\infty} gp(g)dg = 0$ . According to the Law of Large Numbers, when  $k \rightarrow \infty$ , we have  $E[g] = \bar{g} = 0$ . Moreover,  $D[g] = E[g^2] - (E[g])^2 = E[g^2] = \int_{-\infty}^{+\infty} g^2 p(g)dg$ . Clearly, according to Eq. (13) and Eq. (14),  $D(g) = E[g^2] \neq 1$ , and therefore, when  $k \rightarrow \infty$ ,  $D(g) = S_g^2 \neq 1$ .  $\square$

Thm. 3 indicates that the introduction of the no-sampling intervals theoretically does not alter the sample mean  $\bar{g}$  of  $g$ , primarily due to the symmetry of our interval partitioning strategy proposed in Sec. IV-B. However, it potentially induces a change in its sample variance  $S_g^2$ . Therefore, we only need to correct  $S_g^2$  to meet the three conditions mentioned above. To this end, we design a variance-preserving algorithm, the essence of which lies in iteratively adjusting the sampling intervals of  $u$  to ensure that  $S_u^2$  converges to 1. To be more specific, if  $S_u^2 > 1$ , we iteratively reduce the sample variance  $S_u^2$  of  $u$ ; otherwise, we iteratively increase  $S_u^2$ . Fig. 3 presents two examples of  $l = 2$  w.r.t. modes I and II, respectively, illustrating how to increase and decrease  $S_u^2$  during each iteration. The complete implementation of our adjustable PA-B2G is given in Alg. 3, and its reverse process is the same as Alg. 2. Combining Alg. 3 and Fig. 3, it can be seen that in fact, MN, MB, MC, and Multi-bits [22] are four special forms of our PA-B2G.

In Alg. 3, we treat  $h$  not as a hyperparameter, but instead utilize  $\Delta_g$  to dynamically determine the neighborhoods (referred to as no-sampling intervals) around each quantile. The rationale behind this is as follows: If we consider the quantile as a continuous variable  $q$ , for one thing, as  $q \rightarrow 0$  or 1,  $\mathcal{C}_g(q + h) - \mathcal{C}_g(q - h)$  gradually increases, significantly disrupting the normality of  $g$ ; for another, when  $g = \mathcal{C}_g(u)$  undergoes a slight numerical change  $\Delta_g$ , we observe  $\Delta_u \approx \frac{d\mathcal{C}_g^{-1}}{dg} \Delta_g$ . As  $\mathcal{C}_g$  is the PPF of  $\mathcal{N}(0, 1)$ ,  $\frac{d\mathcal{C}_g^{-1}}{dg}$  is a symmetric function that initially increases and then decreases within its domain. Consequently, as  $q \rightarrow 0$  or 1,  $\frac{d\mathcal{C}_g^{-1}}{dg} \rightarrow 0$ , leading to  $\Delta_u \rightarrow 0$ . This suggests that overly long no-sampling intervals are unnecessary for  $q \rightarrow 0$  or 1. Based on this, we directly introduce a hyperparameter  $\Delta_g$  to adjust the deviation of  $g$  from  $\mathcal{N}(0, \mathbf{I})$ , achieving adaptive control of the length of the no-sampling intervals. As shown in fig. 3 and Thm. 3, given a  $\Delta_g$ , as  $q \rightarrow 0$  or 1, both  $h_1, h_2 \rightarrow 0$ , aligning seamlessly with our perspective.

---

### Algorithm 3 Variance-Preserving Algorithm.

---

**Input:** Secret message  $\mathbf{m}$ , maximum iteration steps  $N_{max}$ , and error tolerance  $e$ .  
**Output:** Sampling result  $\mathbf{g}$ .

- 1: Initialize  $c_1 = c_2 = 0$ ;
- 2: Generate a seed sequence  $s_1 \dots s_k$ .
- 3: **for**  $i = 1$  to  $k$  **do**
- 4:     Sample  $r_i \sim \mathcal{U}(0, 1)$  with seed  $s_i$ ;
- 5:     ▷ mode I
- 6:      $h_1 = \frac{m_i+1}{2^l} - \mathcal{C}_g^{-1}(\mathcal{C}_g(\frac{m_i+1}{2^l}) - \Delta_g)$ ;
- 7:      $h_2 = \mathcal{C}_g^{-1}(\mathcal{C}_g(\frac{m_i}{2^l}) + \Delta_g) - \frac{m_i}{2^l}$ ;
- 8:      $u_i = (\frac{1}{2^l} - h_1 - h_2 - c_1 - c_2)r_i + \frac{m_i}{2^l} + h_2$ ;
- 9:      $u_i = u_i + c_1$  **if**  $\frac{m_i}{2} < \frac{1}{2}$  **else**  $u_i + c_2$ ;
- 10:     ▷ mode II
- 11:      $h_1 = \frac{(m_i+1) \bmod 2^l}{2^{l+1}} - \mathcal{C}_g^{-1}(\mathcal{C}_g(\frac{(m_i+1) \bmod 2^l}{2^{l+1}}) - \Delta_g)$ ;
- 12:      $h_2 = \mathcal{C}_g^{-1}(\mathcal{C}_g(\frac{m_i}{2^{l+1}}) + \Delta_g) - \frac{m_i}{2^{l+1}}$ ;
- 13:      $u_i = (\frac{1}{2^{l+1}} - h_1 - h_2 - c_1 - c_2)r_i + \frac{m_i}{2^{l+1}} + h_2 + c_1$  or  
 $u_i = (\frac{1}{2^{l+1}} - h_1 - h_2 - c_1 - c_2)r_i + 1 - \frac{m_i+1}{2^{l+1}} + h_2 + c_2$ ;
- 14: **for**  $step = 1$  to  $N_{max}$  **do**
- 15:      $\mathbf{g} = \mathcal{C}_g(\mathbf{u})$  and calculate  $S_g^2$ ;
- 16:     **if**  $1 - S_g^2 > e$  **then**
- 17:          $c_1 = c_1 + \Delta_c$ ;
- 18:     **else if**  $S_g^2 - 1 > e$  **then**
- 19:          $c_2 = c_2 + \Delta_c$ ;
- 20:     **else** break;
- 21:     Repeat lines 3-13;
- 22: **Return**  $\mathbf{g}$ .

---

#### D. Message Hiding and Extraction with PF-ODEs

After obtaining the standard Gaussian noise  $\mathbf{g}$  generated from  $\mathbf{m}$  with PA-B2G, one can further reparameterize  $\mathbf{g}$  such that  $\mathbf{g} \sim \mathcal{N}(\mathbf{0}, \sigma(T)^2 \mathbf{I})$ . The process of generating a stego image  $\mathbf{x}_0$  from  $\mathbf{g}$  is essentially a problem of numerical integration. There are many ODE solvers applied for DMs. In this paper, we primarily apply the Heun sampler [30] for stego image generation and initial noise retrieval for the following reasons: **i) Universality.** [30] offers a generalized ODE formulation Eq. (2) that is adapted to most existing DMs with different noise schedulers, such as, DDIM [24], VP-SDE [29], and VE-SDE [29], without any training or finetuning. **ii) Efficiency.** Typically, higher-order ODE solvers introduce less local error but also increase the computational cost. To achieve a better computational tradeoff, [30] proposes a 2<sup>nd</sup> order ODE solver for DMs defined on continuous time  $t$ .

However, in practice, directly adapting the Heun sampler to DMs defined on discretized time may cause numerical calculation errors. For example, in the case of adopting the noise scheduler of DDPM,  $\sigma(t) = t = \sqrt{1 - \bar{\alpha}_t}$ , where  $\bar{\alpha}_t$  is a transformed noise scheduler defined in [26]. This creates a problem: when we attempt to retrieve  $\mathbf{g}$  from  $\mathbf{x}_0$ , Heun sampler will fail because the initial noise parameter  $\sigma(0) = \sqrt{1 - \bar{\alpha}_0} = 0$  (see the deterministic sampler defined in [30] for details). To address this problem, we propose to retrieves  $\mathbf{g}$  from  $\mathbf{x}_\epsilon$  instead of  $\mathbf{x}_0$ , where  $\epsilon$  is a small number, e.g.,  $\epsilon = 1e-6$  used in this paper. This modification does

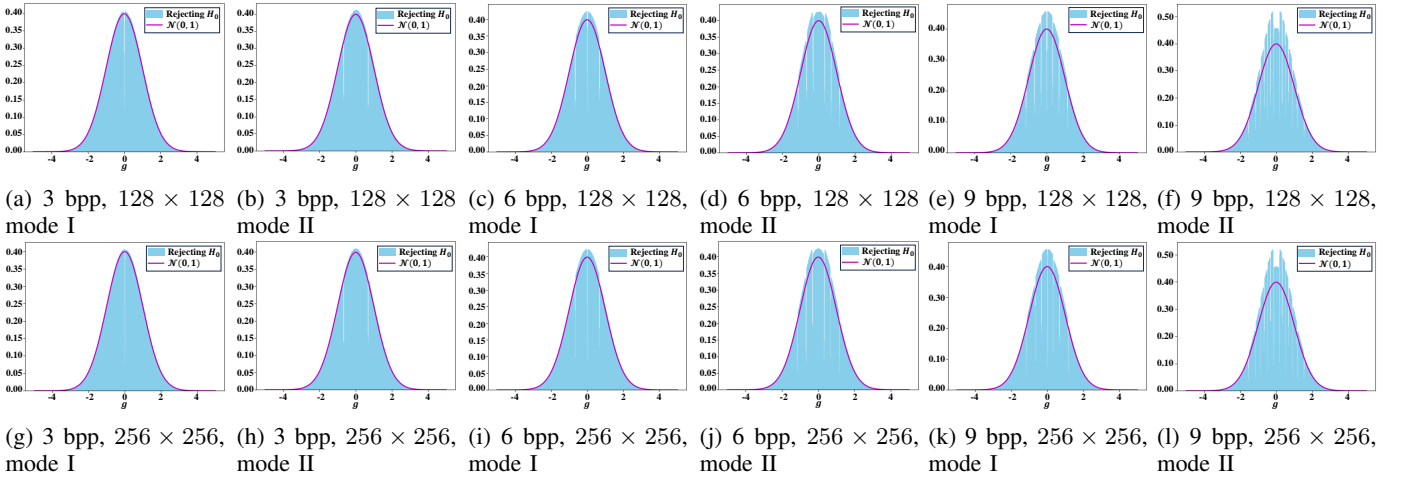


Fig. 4: Averaged histograms of noise that rejecting  $H_0$  w.r.t. different payloads and noise sizes under  $\Delta_g = 0.02$ .

not impact the generation of stego images and enhances the stability of message extraction.

## V. EXPERIMENTS

### A. Experimental setup

**Metrics.** We assess our DGS algorithm's performance using four criteria: visual quality, steganographic security, message extraction accuracy, and embedding capacity.

- Visual quality is evaluated using the Fréchet Inception Distance (FID) score, computed across 50,000 stego images.
- Steganographic security is measured by detection accuracy ( $Acc_s$ ) using the state-of-the-art steganalyzer UCNet [6], with 5,000 cover-stego image pairs for training and 1,000 pairs for testing. Note that the cover images are also generated by generative models but do not contain any hidden secret messages.
- Message extraction accuracy is measured by the average accuracy ( $\bar{Acc}$ ), calculated over 1,000 stego images.
- Embedding capacity is measured in bits per pixel (bpp), calculated as  $\frac{|b|}{h \times w}$ , where  $h$  and  $w$  represent the image height and width, respectively.

**Setup of PA-B2G.** In cases of low payloads, we automatically pads secret bit sequences with either “0” or “1” to match their size with that of generated images. For the following experiments, we set the maximum iteration steps  $N_{max} = 100$  and the correction step size  $\Delta_c = \frac{1}{3072}$ .

### B. Normality Test

We employ the one-sample Kolmogorov-Smirnov (K-S) test to assess the normality of samples generated by PA-B2G. For each sample, we test the null hypothesis  $H_0$  that it comes from  $\mathcal{N}(0, 1)$  against the alternative hypothesis  $H_1$ . A  $p$ -value below 0.05 rejects  $H_0$ ; otherwise, it is accepted. Through a random generation process, we create 1000 samples and compute the ratio  $\frac{N_{H_0}}{1000}$ , where  $N_{H_0}$  denotes the count of samples accepting  $H_0$ . Table I shows the test results w.r.t. varying  $\Delta_g \in \{0, 0.02\}$  and payloads 3 bpp, 6 bpp, 9 bpp

Noise Size( $\times 3$ )	3 bpp		6 bpp		9 bpp		
	Mode I	Mode II	Mode I	Mode II	Mode I	Mode II	
$\Delta_g$	32 × 32	0.957	0.952	0.959	0.954	0.952	0.951
	64 × 64	0.949	0.947	0.951	0.952	0.948	0.950
	128 × 128	0.947	0.949	0.947	0.953	0.950	0.945
	256 × 256	0.946	0.950	0.949	0.951	0.951	0.948
$\Delta_g = 0.02$	32 × 32	0.849	0.872	0.835	0.844	0.845	0.795
	64 × 64	0.405	0.601	0.431	0.401	0.393	0.333
	128 × 128	0.00	0.00	0.00	0.00	0.00	0.00
	256 × 256	0.00	0.00	0.00	0.00	0.00	0.00

TABLE I: Normality test of samples generated by PA-B2G in modes I and II with four different sample sizes w.r.t. varying payloads and  $\Delta_g$ .

for both modes I and II. As we can see, when not introducing the no-sampling intervals (*i.e.*,  $\Delta_g = 0$ ), samples generated by PA-B2G for any noise size and payload almost adhere to  $\mathcal{N}(0, 1)$ . However, despite  $\Delta_g$  is a small number, the ratio  $\frac{N_{H_0}}{1000}$  significantly decrease, especially for large noise size. This may be because the normality of samples generated by PA-B2G is highly sensitive to  $\Delta_g$ , while, on the other hand, the sensitivity of K-S test improves with the sample scale increasing. Furthermore, we depict the averaged histograms of noise that reject  $H_0$  at varying payloads and noise sizes when  $\Delta_g = 0.02$  in Fig. 4. As illustrated, as the payload increases, the distribution of  $g$  will gradually deviate from  $\mathcal{N}(0, 1)$ . However, for low payloads, even though  $H_0$  is rejected, these histograms still closely resemble those of noise sampled from  $\mathcal{N}(0, 1)$ .

### C. Comparison with Prior Work

1) *Comparison with Prior Message Mapping Methods:* We compare our PA-B2G with existing message mapping methods in DGS settings, including MN, MB, MC, and Multi-bits proposed in [22], and GSD [23]. All message mapping methods are evaluated on CIFAR-10 32 × 32, FFHQ 64 × 64, and LSUN-Bedroom 256 × 256 datasets. For each dataset, we equip each mapping method with the same DM and sampling scheduler. To be specific, we employ Heun's 2<sup>nd</sup> order sampler

Method	CIFAR-10 32 × 32						FFHQ 64 × 64						LSUN-Bedroom 256 × 256						
	3 bpp			6 bpp			3 bpp			6 bpp			3 bpp			6 bpp			
	FID↓	$\bar{Acc}$ ↑	$Acc_s$ ↓	FID↓	$\bar{Acc}$ ↑	$Acc_s$ ↓	FID↓	$\bar{Acc}$ ↑	$Acc_s$ ↓	FID↓	$\bar{Acc}$ ↑	$Acc_s$ ↓	FID↓	$\bar{Acc}$ ↑	$Acc_s$ ↓	FID↓	$\bar{Acc}$ ↑	$Acc_s$ ↓	
MN [22]	2.02	83.86%	50.60%	-	-	-	2.46	86.22%	50.83%	-	-	-	10.21	79.46%	49.95%	-	-	-	
MB [22]	2.64	94.36%	92.35%	-	-	-	4.16	98.12%	99.70%	-	-	-	10.98	<b>96.89%</b>	99.90%	-	-	-	
MC [22]	2.25	84.96%	67.00%	-	-	-	3.10	92.70%	97.15%	-	-	-	10.82	82.39%	99.20%	-	-	-	
Multi-bits [22]	-	-	-	2.37	<b>83.01%</b>	74.80%	-	-	-	3.30	<b>90.57%</b>	98.85%	-	-	-	-	-	10.90 <b>80.90%</b>	99.90%
GSD [23]	2.98	<b>98.89%</b>	93.95%	-	-	-	3.08	<b>98.81%</b>	98.85%	-	-	-	10.89	94.11%	99.10%	-	-	-	
PA-B2G <sup>1</sup> (.00)	<b>1.97</b>	84.10%	<b>50.49%</b>	2.03	75.60%	50.75%	2.45	86.85%	50.58%	2.46	79.25%	50.65%	<b>10.19</b>	79.46%	49.74%	<b>10.20</b>	71.12%	<b>49.50%</b>	
PA-B2G <sup>1</sup> (.08)	2.19	88.16%	56.30%	2.17	80.02%	56.82%	2.95	92.76%	79.95%	2.98	88.40%	79.85%	10.75	86.10%	72.75%	10.78	78.10%	72.35%	
PA-B2G <sup>2</sup> (.00)	2.01	75.64%	50.75%	<b>2.00</b>	69.11%	<b>50.43%</b>	<b>2.40</b>	79.22%	<b>50.43%</b>	<b>2.43</b>	70.90%	<b>50.55%</b>	10.21	72.14%	<b>48.80%</b>	10.21	62.54%	49.80%	
PA-B2G <sup>2</sup> (.08)	2.13	80.99%	53.80%	2.08	71.53%	53.40%	2.94	88.35%	79.50%	2.89	77.16%	79.60%	10.71	82.87%	71.80%	10.73	71.90%	72.30%	

TABLE II: Comparison with existing message mapping methods using metrics FID,  $Acc_s$ , and,  $\bar{Acc}$  on CIFAR-10  $32 \times 32$ , FFHQ  $64 \times 64$ , and LSUN-Bedroom  $256 \times 256$  datasets under various payloads. PA-B2G<sup>1</sup>(.00) denotes PA-B2G in mode I with  $\Delta_g = 0.00$ , and others follow similarly.

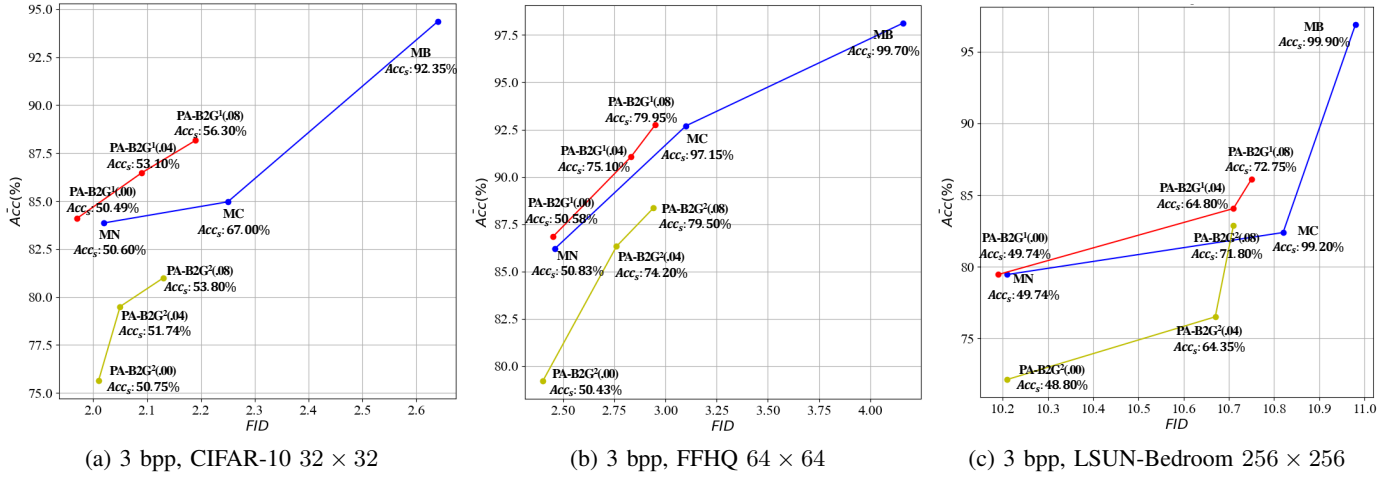


Fig. 5: Visualization results of the adjustment strategies adopted by [22] and PA-B2G on CIFAR-10, FFHQ, and LSUN-Bedroom.

Method	3 bpp			6 bpp			9 bpp		
	FID↓	$\bar{Acc}$ ↑	$Acc_s$ ↓	FID↓	$\bar{Acc}$ ↑	$Acc_s$ ↓	FID↓	$\bar{Acc}$ ↑	$Acc_s$ ↓
GSF [15]	25.02	<b>91.98%</b>	51.87%	44.17	73.47%	99.73%	51.80	62.85%	99.87%
GSN [12]	16.11	74.31%	99.80%	17.02	60.75%	99.47%	19.98	52.25%	99.54%
S2IRT [16]	44.52	50.10%	99.85%	45.74	50.47%	99.90%	-	-	-
PA-B2G <sup>1</sup> (.08)	<b>7.70</b>	90.81%	<b>51.75%</b>	<b>7.68</b>	<b>80.89%</b>	<b>52.45%</b>	<b>7.72</b>	<b>72.88%</b>	<b>50.90%</b>

TABLE III: Comparison with GAN-based and Flow-based GS methods using metrics FID,  $Acc_s$ , and,  $\bar{Acc}$  on CelebA  $64 \times 64$  under various payloads. PA-B2G<sup>1</sup>(.08) denotes PA-B2G in mode I with  $\Delta_g = 0.08$ .

for CIFAR-10  $32 \times 32$  with 20 sampling steps and FFHQ  $64 \times 64$  with 42 sampling steps, while using DDIM's 1<sup>st</sup> order sampler for LSUN-Bedroom  $256 \times 256$  with 18 sampling steps. We set the error tolerance  $e = 0.0185$  defined in Alg. 3 for CIFAR-10  $32 \times 32$  and FFHQ  $64 \times 64$ , and  $e = 0.007$  for LSUN-Bedroom  $256 \times 256$ . Before being hidden, all secret bits are padded and then encrypted as necessary to meet required payloads. All mapping methods utilize the same set of random seeds for stego image generation, and the corresponding generated images are saved in PNG format.

We report the FID score,  $\bar{Acc}$ , and  $Acc_s$  for each message mapping method at different payloads in Table II. As shown,

previous message mapping methods, such as MB, MC, Multi-bits, and GSD, all fail to provide the claimed security when faced with the color image steganalyzer [6]. Most of these methods can be easily detected (i.e.,  $Acc_s > 95\%$ ), especially at high payloads. This vulnerability arises because these methods significantly alter the initial noise distribution of DMs for message hiding without considering its correlation with steganographic security, as discussed in Sec. IV-A. Additionally, these methods lack flexibility across different payloads and are only suitable for specific payloads. In contrast, our PA-B2G method offers flexible adaptation between low and high payloads. It achieves state-of-the-art image quality and steganographic security by adjusting  $\Delta_g$ , with only a minor decrease in extraction accuracy across various payloads and datasets. Additionally, we find that PA-B2G in mode II has lower message extraction accuracy compared to mode I, primarily due to the introduction of additional quantiles.

2) *Comparison with GAN- and Flow-based Methods:* We also compare PA-B2G with two flow-based methods, GSF [15] and S2IRT [16], and a GAN-based method, GSN [12], on the CelebA  $64 \times 64$  dataset at payloads ranging from 3 bpp to 9 bpp. GSF and S2IRT utilize the same pre-trained Glow

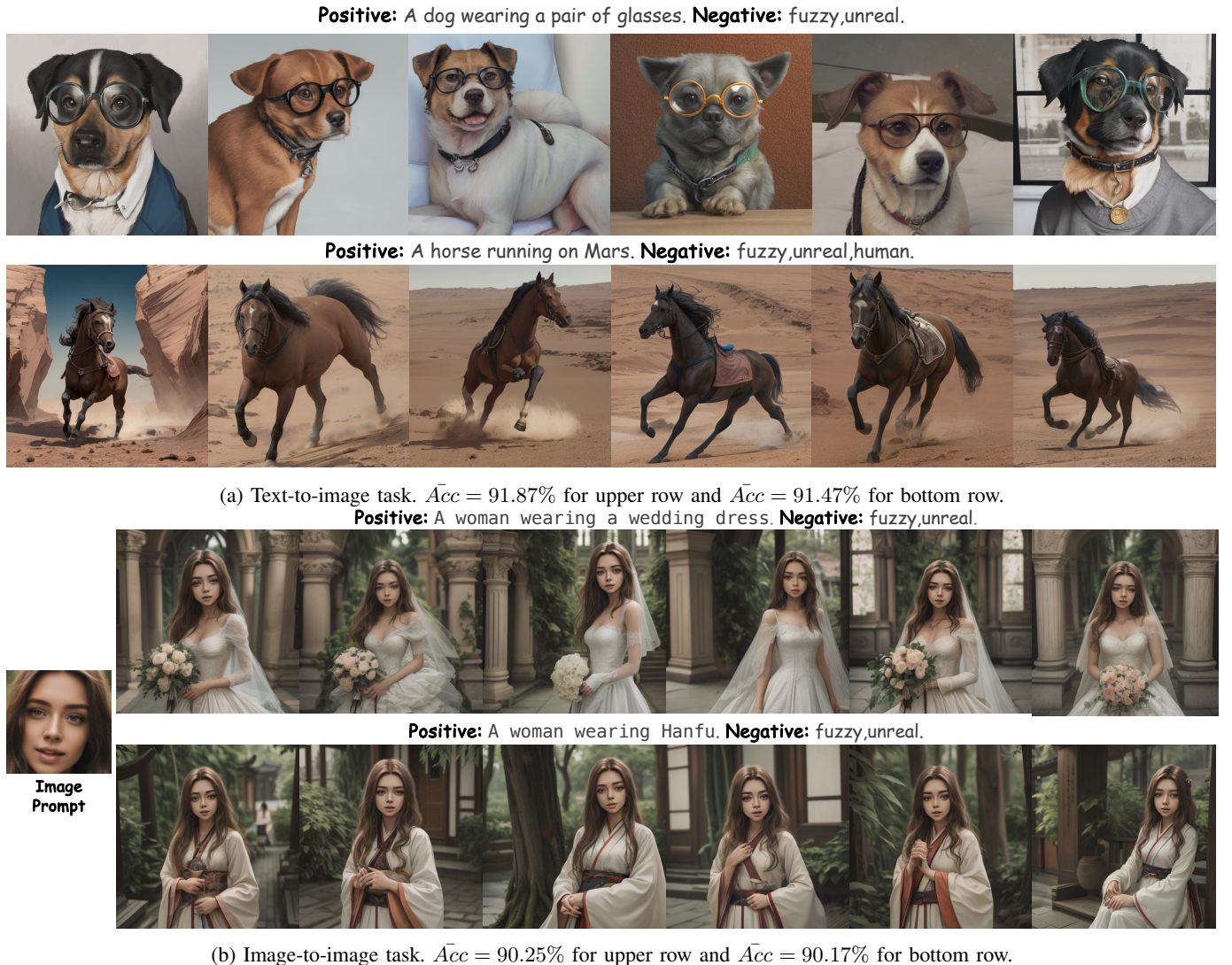


Fig. 6: Visualization results of combining PA-B2G in mode I with the Stable Diffusion on text-to-image task and image-to-image task.

model<sup>2</sup>. For S2IRT, to ensure computational efficiency, we set the group number  $K$  to 30 for a payload of 3 bpp and to 40 for 6 bpp. For higher payloads, S2IRT requires a larger  $K$ , but it becomes too time-consuming to generate 50,000 stego images, so we do not report its corresponding results in Table III. Since PA-B2G in mode I is superior to mode II in message extraction accuracy, we selected it with  $\Delta_g = 0.08$  and  $e = 0.007$  for comparison. We use the pre-trained DM from DDIM [24], but replace its sampling scheduler with Heun's 2nd order sampler, as suggested in Sec. IV-D. The relevant comparison results are presented in Table III. As shown, our PA-B2G significantly outperforms other GS methods, especially in image quality and steganographic security, primarily due to the powerful generation capability of DMs and our careful modification of the initial DM noise.

3) *Comparison with Prior Adjustment Strategies.:* Kim *et al.* [22] have experimentally verified that there exists a trade-off between image quality and message extraction accuracy,

proposing three options, namely MN, MB, and MC, to adjust such trade-off. To validate the effectiveness of the adjustment strategy proposed in Alg. 3, we report the FID score,  $\bar{Acc}$ , and  $\bar{Acc}_s$  of MN, MC, MB, and PA-B2G in modes I and II with varying  $\Delta_g$  in Table II. To illustrate the adjustability of PA-B2G more intuitively, we further provide more adjustment results in Fig. 5. The results confirm the existence of a trade-off among the image quality, steganographic security, and extraction accuracy, demonstrating that we can effectively balance them by adjusting  $\Delta_g$ . This further validates our analysis in Sec. IV-A. Fig. 5 also shows that our adjustment strategy is more natural and fine-grained than the one proposed in [22]. By changing  $\Delta_g$ , we can readily achieve FID scores,  $\bar{Acc}$ , and  $\bar{Acc}_s$  close to those of MN, MC, and MB, as they are merely special cases of our PA-B2G.

#### D. Combining with Modern Latent DMs

In previous experiments, the DMs used are all trained in color space. In this section, we further evaluate the compati-

<sup>2</sup><https://github.com/chaiyujin/glow-pytorch.git>

Method	32 × 32 × 3		64 × 64 × 3		128 × 128 × 3	
	3 bpp	6 bpp	3 bpp	6 bpp	3 bpp	6 bpp
PA-B2G <sup>1</sup> (.00)	0.004s	0.005s	0.015s	0.016s	0.061s	0.084s
PA-B2G <sup>1</sup> (.04)	0.018s	0.022s	0.054s	0.089s	0.193s	0.306s
PA-B2G <sup>1</sup> (.08)	0.043s	0.049s	0.148s	0.222s	0.520s	0.871s
PA-B2G <sup>2</sup> (.00)	0.005s	0.007s	0.025s	0.029s	0.084s	0.119s
PA-B2G <sup>2</sup> (.04)	0.020s	0.025s	0.071s	0.074s	0.217s	0.264s
PA-B2G <sup>2</sup> (.08)	0.046s	0.057s	0.171s	0.177s	0.725s	0.784s

TABLE IV: Average time consumption for hiding secret bits into the initial DM noise of different sizes using PA-B2G. PA-B2G<sup>1</sup>(.00) denotes PA-B2G in mode I with  $\Delta_g = 0.00$ , and others follow similarly.

bility of our PA-B2G with Stable Diffusion [19], currently the most popular conditional DM trained in latent space. We test our PA-B2G on two common image generation tasks: text-to-image and image-to-image. For the text-to-image task, we use Dreamshaper 7<sup>3</sup>, which is fine-tuned on Stable Diffusion 1.5, as the foundational generative model, along with Heun’s 2nd order sampler for stego image generation. PA-B2G in mode I is selected for message mapping due to its superior performance in extraction accuracy. For the image-to-image task, we utilize IP-Adapter [33] to encode image prompts and Dreamshaper 7 as the foundational generative model. For each task, each text prompt consist of a positive prompt and a negative prompt. The error tolerance  $e$  is set to 0.02, code length  $l$  to 1,  $\Delta_g$  to 0.08, the guidance scale to 1.5, and the number of sampling steps to 50. Given that the latent initial noise has dimensions of  $64 \times 64 \times 4$  and the generated images have dimensions of  $512 \times 512 \times 3$ , the payload is approximately equal to 0.0208 bpp. The corresponding image quality and message extraction accuracy are reported in Fig. 6. As illustrated, PA-B2G maintains excellent generation performance while achieving an extraction accuracy exceeding 90% across both image generation tasks. This underscores its capability to be seamlessly integrated with conditional latent DMs for effective information hiding, highlighting its considerable practical application potential.

### E. Computational Complexity

This section discusses the computational complexity of our PA-B2G in Modes I and II. Our complete message-hiding process comprises four steps: transforming secret bits  $\mathbf{b}$  to Gaussian noise  $\mathbf{g}$ , reverse ODE sampling, forward ODE sampling, and recovering  $\mathbf{b}$  from  $\mathbf{g}$ . For the first step, we report PA-B2G’s average time taken to hide secret bits into the initial DM noise of various sizes in Table IV. The error tolerance  $e$  is uniformly set to 0.0185. As shown, as the noise size and  $\Delta_g$  increase, PA-B2G in Modes I and II consumes more time. This can be alleviated by appropriately increasing the correction step  $\Delta_c$  or the error tolerance  $e$ . However, regardless of the mode or noise size, PA-B2G consistently completes the first step in under 1 second. For the diffusion sampling step, which includes reverse and forward ODE sampling, the time consumption depends on the sampling steps, DM size,

and noise size. However, this is beyond the scope of our investigation in this paper. The time taken to transform  $\mathbf{g}$  back to  $\mathbf{b}$  is significantly less than that of its reverse counterpart, and thus we do not report it here.

## VI. CONCLUSION

In this paper, we explore a trade-off among image quality, steganographic security, and extraction accuracy in DGS settings. We identify the normality of initial DM noise as pivotal in this triadic relationship. Theoretical and experimental analyses reveal that any message mapping method compromising normality significantly reduces steganographic security and marginally impacts image quality. In response, we propose PA-B2G, which can reversibly encodes any secret messages into Gaussian-distributed noise. Our experimental findings demonstrate its superior ability to finely balance image quality, steganographic security, and extraction accuracy. Moreover, PA-B2G can seamlessly integrate into pre-trained deep models for realistic stego image generation. However, some issues remain unaddressed in this paper. For instance, in DGS settings, existing message mapping methods, including PA-B2G, lack robustness against JPEG compression, blurring, and other image attacks, diminishing their practical value. Future work will aim to enhance the robustness of our GS algorithm against these image attacks through deep model refinement. Additionally, exploring the potential use of PA-B2G for DM watermarking is another worthwhile avenue for research.

## REFERENCES

- [1] W. Luo, F. Huang, and J. Huang, “Edge adaptive image steganography based on lsb matching revisited,” *IEEE Transactions on Information Forensics and Security*, vol. 5, no. 2, pp. 201–214, 2010.
- [2] T. Filler, J. Judas, and J. Fridrich, “Minimizing additive distortion in steganography using syndrome-trellis codes,” *IEEE Transactions on Information Forensics and Security*, vol. 6, no. 3, pp. 920–935, 2011.
- [3] J. Fridrich and J. Kodovsky, “Rich models for steganalysis of digital images,” *IEEE Transactions on Information Forensics and Security*, vol. 7, no. 3, pp. 868–882, 2012.
- [4] G. Xu, H.-Z. Wu, and Y.-Q. Shi, “Structural design of convolutional neural networks for steganalysis,” *IEEE Signal Processing Letters*, vol. 23, no. 5, pp. 708–712, 2016.
- [5] W. You, H. Zhang, and X. Zhao, “A siamese cnn for image steganalysis,” *IEEE Transactions on Information Forensics and Security*, vol. 16, pp. 291–306, 2020.
- [6] K. Wei, W. Luo, S. Tan, and J. Huang, “Universal deep network for steganalysis of color image based on channel representation,” *IEEE Transactions on Information Forensics and Security*, vol. 17, pp. 3022–3036, 2022.
- [7] M.-m. Liu, M.-q. Zhang, J. Liu, Y.-n. Zhang, and Y. Ke, “Coverless information hiding based on generative adversarial networks,” *arXiv preprint arXiv:1712.06951*, 2017.
- [8] D. Hu, L. Wang, W. Jiang, S. Zheng, and B. Li, “A novel image steganography method via deep convolutional generative adversarial networks,” *IEEE Access*, vol. 6, pp. 38303–38314, 2018.
- [9] Z. Wang, N. Gao, X. Wang, X. Qu, and L. Li, “Sstegan: self-learning steganography based on generative adversarial networks,” in *Neural Information Processing: 25th International Conference, ICONIP 2018, Siem Reap, Cambodia, December 13–16, 2018, Proceedings, Part II 25*. Springer, 2018, pp. 253–264.
- [10] C. Yu, D. Hu, S. Zheng, W. Jiang, M. Li, and Z.-q. Zhao, “An improved steganography without embedding based on attention gan,” *Peer-to-Peer Networking and Applications*, vol. 14, pp. 1446–1457, 2021.
- [11] X. Liu, Z. Ma, J. Ma, J. Zhang, G. Schaefer, and H. Fang, “Image disentanglement autoencoder for steganography without embedding,” in *Proceedings of the IEEE/CVF conference on computer vision and pattern recognition*, 2022, pp. 2303–2312.

<sup>3</sup><https://huggingface.co/Lykon/dreamshaper-7>

- [12] P. Wei, S. Li, X. Zhang, G. Luo, Z. Qian, and Q. Zhou, "Generative steganography network," in *Proceedings of the 30th ACM International Conference on Multimedia*, 2022, pp. 1621–1629.
- [13] Z. Ma, Y. Zhu, G. Luo, X. Liu, G. Schaefer, and H. Fang, "Robust steganography without embedding based on secure container synthesis and iterative message recovery," in *IJCAI*, 2023, pp. 4838–4846.
- [14] Z. Zhou, X. Dong, R. Meng, M. Wang, H. Yan, K. Yu, and K.-K. R. Choo, "Generative steganography via auto-generation of semantic object contours," *IEEE Transactions on Information Forensics and Security*, 2023.
- [15] P. Wei, G. Luo, Q. Song, X. Zhang, Z. Qian, and S. Li, "Generative steganographic flow," in *2022 IEEE International Conference on Multimedia and Expo*. IEEE, 2022, pp. 1–6.
- [16] Z. Zhou, Y. Su, J. Li, K. Yu, Q. J. Wu, Z. Fu, and Y. Shi, "Secret-to-image reversible transformation for generative steganography," *IEEE Transactions on Dependable and Secure Computing*, 2022.
- [17] I. Goodfellow, J. Pouget-Abadie, M. Mirza, B. Xu, D. Warde-Farley, S. Ozair, A. Courville, and Y. Bengio, "Generative adversarial networks," *Communications of the ACM*, vol. 63, no. 11, pp. 139–144, 2020.
- [18] D. P. Kingma and P. Dhariwal, "Glow: Generative flow with invertible 1x1 convolutions," *Advances in neural information processing systems*, vol. 31, 2018.
- [19] R. Rombach, A. Blattmann, D. Lorenz, P. Esser, and B. Ommer, "High-resolution image synthesis with latent diffusion models," in *Proceedings of the IEEE/CVF conference on computer vision and pattern recognition*, 2022, pp. 10 684–10 695.
- [20] C. Saharia, W. Chan, S. Saxena, L. Li, J. Whang, E. Denton, S. K. S. Ghasemipour, B. K. Ayan, S. S. Mahdavi, R. G. Lopes, T. Salimans, J. Ho, D. J. Fleet, and M. Norouzi, "Photorealistic text-to-image diffusion models with deep language understanding," 2022. [Online]. Available: <https://arxiv.org/abs/2205.11487>
- [21] A. Ramesh, P. Dhariwal, A. Nichol, C. Chu, and M. Chen, "Hierarchical text-conditional image generation with clip latents," *arXiv preprint arXiv:2204.06125*, vol. 1, no. 2, p. 3, 2022.
- [22] D. Kim, C. Shin, J. Choi, D. Jung, and S. Yoon, "Diffusion-stego: Training-free diffusion generative steganography via message projection," *arXiv preprint arXiv:2305.18726*, 2023.
- [23] P. Wei, Q. Zhou, Z. Wang, Z. Qian, X. Zhang, and S. Li, "Generative steganography diffusion," *arXiv preprint arXiv:2305.03472*, 2023.
- [24] J. Song, C. Meng, and S. Ermon, "Denoising diffusion implicit models," in *International Conference on Learning Representations*, 2020.
- [25] Y. Peng, D. Hu, Y. Wang, K. Chen, G. Pei, and W. Zhang, "Stegad-dpm: Generative image steganography based on denoising diffusion probabilistic model," in *Proceedings of the 31st ACM International Conference on Multimedia*, 2023, pp. 7143–7151.
- [26] J. Ho, A. Jain, and P. Abbeel, "Denoising diffusion probabilistic models," *Advances in neural information processing systems*, vol. 33, pp. 6840–6851, 2020.
- [27] R. T. Chen, Y. Rubanova, J. Bettencourt, and D. K. Duvenaud, "Neural ordinary differential equations," *Advances in neural information processing systems*, vol. 31, 2018.
- [28] Y. Song and S. Ermon, "Generative modeling by estimating gradients of the data distribution," *Advances in neural information processing systems*, vol. 32, 2019.
- [29] Y. Song, J. Sohl-Dickstein, D. P. Kingma, A. Kumar, S. Ermon, and B. Poole, "Score-based generative modeling through stochastic differential equations," in *International Conference on Learning Representations*, 2020.
- [30] T. Karras, M. Aittala, T. Aila, and S. Laine, "Elucidating the design space of diffusion-based generative models," *Advances in Neural Information Processing Systems*, vol. 35, pp. 26 565–26 577, 2022.
- [31] Y. Ke, M.-q. Zhang, J. Liu, T.-t. Su, and X.-y. Yang, "Generative steganography with kerckhoffs' principle," *Multimedia Tools and Applications*, vol. 78, no. 10, pp. 13 805–13 818, 2019.
- [32] C. Cachin, "An information-theoretic model for steganography," in *International Workshop on Information Hiding*. Springer, 1998, pp. 306–318.
- [33] H. Ye, J. Zhang, S. Liu, X. Han, and W. Yang, "Ip-adapter: Text compatible image prompt adapter for text-to-image diffusion models," *arXiv preprint arXiv:2308.06721*, 2023.